



Three-dimensional hierarchical SnO₂ dodecahedral nanocrystals with enhanced humidity sensing properties

Honglei Feng¹, Chen Li¹, Tao Li, Feiyu Diao, Tuo Xin, Bin Liu, Yiqian Wang*

College of Physics, Qingdao University, No. 308 Ningxia Road, Qingdao, 266071, People's Republic of China

ARTICLE INFO

Article history:

Received 12 August 2016

Received in revised form 9 December 2016

Accepted 9 December 2016

Available online 10 December 2016

Keywords:

Morphology

Surface

Humidity sensing properties

ABSTRACT

One-step hydrothermal method was adopted to synthesize tin dioxide (SnO₂) nanostructures with different morphologies, i.e., three-dimensional (3D) hierarchical SnO₂ dodecahedral nanocrystals (DNCs), 3D hierarchical SnO₂ nanorods (NRs), and SnO₂ nanoparticles (NPs). The humidity sensors based on the as-synthesized nanostructures were produced to investigate the relationship between morphology and humidity sensing property. The nanosensor based on 3D hierarchical SnO₂ DNCs exhibited superior humidity sensing properties compared to those based on 3D hierarchical SnO₂ NRs and SnO₂ NPs. The enhanced sensing properties for SnO₂ DNCs are attributed to the peculiar 3D open nanostructures and high chemical activity of the exposed {101} facets. The 3D open nanostructures can promote the penetration and diffusion of water molecules, and the exposed {101} facets can improve the adsorption ability of water molecules. Furthermore, density functional theory (DFT) calculations were performed to further confirm that {101} facets can adsorb more water molecules than {110} facets. Our results demonstrate that morphology and surface engineering is an effective strategy to enhance the humidity sensing properties of nanomaterials.

© 2016 Elsevier B.V. All rights reserved.

1. Introduction

Since humidity has a great impact on the industrial production, storage of various goods and environmental monitoring, considerable investigations have been carried out to develop suitable humidity-sensitive materials for the fabrication of high-performance humidity sensors. Many types of functional materials such as metal oxides [1], polymers [2,3] and inorganic/organic hybrids [4] have been utilized as humidity sensing materials. Among the various sensing materials, metal oxides have received intensive interest due to their unique properties such as chemical and physical stability, high mechanical strength and wide operating temperature range [5–7].

Tin dioxide (SnO₂) is a versatile semiconductor material which is commonly used in gas sensor [8,9], lithium-ion battery [10] and solar cell [11]. Recently, SnO₂ has emerged as an important humidity sensing material due to its inherent chemical and physical stability [12] and easy adsorption of water in molecu-

lar or hydroxyl form [13]. However, SnO₂ humidity nanosensors displayed very long response and recovery times and low sensitivity [12,14]. Hence, many scientific and technological efforts have been directed towards improving humidity-sensing performance of SnO₂ humidity nanosensors. For example, many semiconductor hetero-contact systems such as TiO₂-SnO₂ [15], WO₃-SnO₂ [16], and RGO-SnO₂ [17] were reported to possess enhanced sensitivity and fast response and recovery times. However, to our knowledge, little information is available in previous reports about enhancing the humidity-sensing properties of SnO₂ through tuning its morphology and surface architecture.

It has been found that the properties of SnO₂ strongly depend on its morphology and shape. For instance, Wang et al. [18] prepared hierarchical flower-like SnO₂ nanospheres assembled from short nanorods (NRs) for potential applications in gas sensing and lithium-ion battery. Zhao et al. [19] synthesized SnO₂ hierarchical architectures to investigate the relationship between the morphology and photocatalytic activities. However, few investigations focus on the correlation between morphology and humidity-sensing properties.

Herein, we synthesized SnO₂ nanostructures with different morphologies including three-dimensional (3D) hierarchical SnO₂ dodecahedral nanocrystals (DNCs), 3D hierarchical SnO₂ NRs and

* Corresponding author.

E-mail address: yqwang@qdu.edu.cn (Y. Wang).

¹ These authors contributed equally to this work.

SnO_2 nanoparticles (NPs) through one-step hydrothermal process, and studied the performance of the humidity sensors based on different SnO_2 nanostructures. Interestingly, in our experiments the sensors realized with 3D SnO_2 nanostructures (DNCs and NRs) showed a response time of less than 4 s and a recovery time of less than 13 s, both significantly superior to the SnO_2 NPs. The fast response and recovery times are attributed to the pore channels present in the 3D SnO_2 nanostructures. Moreover, compared with 3D hierarchical SnO_2 NRs, 3D hierarchical SnO_2 DNCs displayed higher sensitivity with an impressive impedance change of 4.2 orders in 11–95% relative humidity (RH) range. The high sensitivity is ascribed to the exposed {101} facets of 3D hierarchical SnO_2 DNCs which can improve the adsorption ability of water molecules and enhance the humidity sensitivity. Furthermore, density functional theory (DFT) calculations are performed to prove that {101} facets can adsorb more water molecules than {110} facets. This work will pave the way to the development of promising practical humidity sensors.

2. Experimental

All chemicals were of analytical grade and used as received. Distilled water was used throughout the whole experiment.

2.1. Synthesis of 3D hierarchical SnO_2 NRs

3D hierarchical SnO_2 NRs were synthesized by a simple hydrothermal method. Typically, under vigorous stirring, 20 mL of 0.75 mol/L NaOH aqueous solution was added to 20 mL of 0.075 mol/L $\text{SnCl}_4 \cdot 5\text{H}_2\text{O}$ ethanol solution, followed by ultrasonication for 5 min. The above mixture was then transferred into a 100 mL Teflon-sealed autoclave and maintained at 180 °C for 12 h. Subsequently, the resultant precipitates were collected by centrifugation and washed with distilled water and ethanol several times, and then dried at 60 °C for 12 h to obtain SnO_2 product.

2.2. Synthesis of SnO_2 NPs

0.35 g of $\text{SnCl}_4 \cdot 5\text{H}_2\text{O}$ and 0.6 g of benzimidazole were first dissolved into mixed solution with 20 mL distilled water and 20 mL ethanol, and then transferred into a 100 mL Teflon-sealed autoclave at 180 °C for 18 h. Finally, the obtained sample was rinsed with distilled water and ethanol for several times, and dried in air at 60 °C for 12 h.

2.3. Synthesis of 3D hierarchical SnO_2 DNCs

1 mmol $\text{SnCl}_4 \cdot 5\text{H}_2\text{O}$, 10 mmol NaOH and 0.3 g sodium alginate were each dissolved in 20 mL, 20 mL and 30 mL distilled water. After that, NaOH solution was dripped into SnCl_4 solution while stirring to form a homogeneous solution. The mixture was then added into the sodium alginate solution dropwise under stirring and the resulting mixture was put into 100 mL Teflon-sealed autoclave, which was heated at 180 °C for 18 h. After cooling to room temperature, the resultant precipitates were centrifuged and thoroughly washed with distilled water and ethanol several times, and dried in air at 60 °C for 12 h.

2.4. Preparation of TEM samples

TEM samples of SnO_2 nanostructures were prepared by ultrasonication them in ethanol for several minutes, and dispersing a drop onto a holey-carbon-film-coated copper grid.

2.5. Characterization

The morphologies of the as-synthesized samples were characterized by scanning electron microscope (SEM, Hitachi S-4800) and the crystal structures of the samples were analyzed by SmartLab XRD with Cu-K α 1 radiation ($\lambda = 1.5406 \text{ \AA}$). Selected-area electron diffraction (SAED) pattern, bright-field (BF) images, and high-resolution transmission electron microscopy (HRTEM) images were obtained on a JEOL JEM2100F TEM with an accelerating voltage of 200 kV. X-ray photoelectron spectroscopy (XPS) was performed on a Thermo Scientific ESCALAB 250Xi instrument with a monochromatic Al K α radiation ($h\nu = 1486.6 \text{ eV}$) under an ultra-high vacuum (below 10^{-8} Pa). The binding energies were calibrated using C 1s peak (284.8 eV) as a reference.

The nitrogen adsorption-desorption was carried out on an automatic volumetric sorption analyzer (NOVA 1100, Quantachrome, USA) at 77 K. The Brunauer-Emmett-Teller (BET) was used to calculate the specific surface areas of different SnO_2 nanostructures. The pore size distributions were obtained using Barrer-Joyner-Halenda (BJH) method.

2.6. Measurement of humidity sensing properties

Golden interdigital electrodes (10 mm × 10 mm × 0.5 mm) are employed as the basic test component to fabricate the humidity sensors, purchased from Shenzhen Xingshengjie Electronics Co., Ltd (Shenzhen, China). The schematic diagram of the interdigital electrodes is shown in Fig. S1. As shown in Fig. S1, both the width of a finger and the spacing between the adjacent fingers are about 75 μm . Two leading wires are connected with the gold electrodes by soldering of tin. Prior to use, the interdigital electrodes were ultrasonically cleaned in acetone, then rinsed thoroughly with distilled water and dried in vacuum. The test samples were ground and mixed with distilled water (weight ratio 10:1) to obtain a paste. After that, the paste was uniformly coated onto the sensing area of the interdigital electrodes and then dried in air at 60 °C for 12 h. Fig. S2 presents the cross-sectional SEM images of different SnO_2 nanostructures coated on the electrodes, from which it can be seen the coated films have a thickness of ~10 μm . The different RH levels were generated by various saturated salt solutions in the closed glass chambers at room temperature (25 °C). The eight different standard saturated aqueous salt solutions of LiCl, $\text{MgCl}_2 \cdot 6\text{H}_2\text{O}$, K_2CO_3 , $\text{Mg}(\text{NO}_3)_2 \cdot 6\text{H}_2\text{O}$, KI, NaCl, KCl and KNO_3 which yield relative humidities (RHs) of 11%, 33%, 43%, 54%, 69%, 75%, 84% and 95%, respectively, were used to act as humidity sources. The RH levels were monitored by a standard hygrometer. The coated interdigital electrodes were placed successively into the chambers with different RH levels at room temperature and the impedance of the sensors was measured as a function of RH at 25 °C using a precision LCR meter (TH2828, China) and a Metrohm Autolab electrochemical workstation (PGSTAT 302N). To minimize the influence of laboratory climate, the sensors were rapidly switched between the above-mentioned chambers. The applied voltage was alternating current (AC) 1 V, and the frequency varied from 50 Hz to 100 kHz.

2.7. Theoretical calculations

All calculations in the present work were carried out by DMol³ program package in Material Studio [20,21]. Perdew-Burke-Ernzerhof (PBE) of generalized gradient approximation (GGA) was used as exchange-correlation function [22]. The valence orbital of the atoms was described by setting the double-numeric quality with polarization functions (DNP), and DFT semi-core pseudopotentials (DSPPs) were employed to substitute the core electrons

[23,24]. The periodic (3×2) and (2×2) slab models were used to simulate the SnO_2 {110} and {101} surfaces, respectively.

3. Results and discussion

3.1. Characterization of samples

Fig. 1 displays the XRD patterns of the as-synthesized products. All the diffraction peaks can be indexed to tetragonal structure of SnO_2 (JCPDS no. 41-1445). No notable peak of impurities can be detected, which indicates that no other phase was formed. The diffraction peaks of 3D hierarchical SnO_2 NRs and DNCs are sharp and intense, as shown in **Fig. 1(a)** and **(c)**. In contrast to the NRs and DNCs, the broader diffraction peaks of SnO_2 NPs are observed from **Fig. 1(b)**. The average crystallite sizes are ~ 45 nm for NRs, ~ 5 nm for NPs and ~ 24 nm for DNCs, respectively, calculated from (110) peaks using Scherrer equation [25].

Fig. 2 presents SEM images of three different SnO_2 nanostructures. It can be seen from **Fig. 2(a)** that the 3D open nanostructures are assembled from one-dimensional (1D) SnO_2 NRs from their center towards different directions. These NRs are of well-defined quadrangular shape with a diameter of around 50 nm and a length of around 300 nm, as shown in high-magnification SEM image (**Fig. 2(b)**). **Fig. 2(c)** is a typical low-magnification SEM image of the as-synthesized SnO_2 NPs, in which a number of NPs are piled together. **Fig. 2(d)** shows a high-magnification SEM image of SnO_2 NPs, from which it can be seen that the diameter of NPs is 5–10 nm. **Fig. 2(e)** provides a typical SEM image of 3D hierarchical SnO_2 DNCs, from which it can be seen that 3D nanostructures are assembled from nanocrystals with a diameter of 20–30 nm. Close examinations of **Fig. 2(f)** show that these nanocrystals are dodecahedral, whose coping is pyramid-shaped as demonstrated in the inset of **Fig. 2(f)**. Compared with NPs, it can be found that plenty of voids and interspaces are present in both 3D hierarchical NRs and DNCs, thus forming loose and porous 3D structures.

The element compositions of as-synthesized products were examined by XPS. **Fig. 3(a)** shows the XPS profiles of 3D hierarchical SnO_2 DNCs in the range of 0–1200 eV. All the peaks in **Fig. 3(a)** can be ascribed to Sn, O and C, which demonstrate that Sn, O and C elements exist in the SnO_2 DNCs. To study the detailed element compositions of 3D hierarchical SnO_2 DNCs, high-resolution XPS spectra were also performed. As shown in **Fig. 3(b)**, there are two peaks in the Sn 3d region. The peak located at 485.9 eV corresponds to the Sn 3d_{5/2} and the other located at 494.3 eV is assigned to Sn 3d_{3/2} [26]. The splitting gap between the peaks of Sn 3d_{5/2} and Sn 3d_{3/2} is 8.4 eV, indicating a normal state of Sn^{4+} in the as-prepared SnO_2 DNCs. **Fig. 3(c)** presents the XPS spectrum of O 1s, from which it can be seen that the O 1s peak is broad and asymmetric, indicating that there could be more than one chemical state according to the binding energy [15]. Using the XPS peak fitting program, the O 1s spectrum can be fitted by three kinds of chemical states including crystal lattice oxygen (Sn-O), surface hydroxyl group (-OH) and adsorbed water (-H₂O). To compare the element compositions of different SnO_2 nanostructures, the SnO_2 NRs and NPs were also analyzed by XPS. **Fig. S3** shows the XPS spectra of SnO_2 NRs and NPs, in which the O 1s spectra can be fitted using two kinds of chemical states (lattice oxygen and surface OH group). The different kinds of chemical states inferred from the O 1s spectra indicate that less surface OH groups and water molecules are adsorbed on the surface of the SnO_2 NRs and NPs than on the surface of 3D hierarchical SnO_2 DNCs [15].

The microstructures of different SnO_2 nanostructures were extensively examined by TEM. **Fig. 4(a)** displays a typical BF TEM image of 3D hierarchical SnO_2 NRs. Consistent with the above XRD pattern and SEM observation, the 3D SnO_2 nanostructures

are assembled from quadrangular-shape NRs with a diameter of 50 nm and a length of around 300 nm. The crystal lattice spacings measured from the HRTEM image are 3.35 Å and 3.15 Å, as indicated in **Fig. 4(b)**, which correspond to {110} side facets and {001} top facets of nanorod (NR), respectively. The corresponding SAED pattern in **Fig. 4(c)** reveals that the SnO_2 NRs are single crystals and can be indexed to [110] zone-axis of tetragonal SnO_2 . **Fig. 4(d)** displays an atomic model of the ideal SnO_2 cuboid enclosed by {110} and {001} facets projected along the [110] direction. It can be seen that the outline of the SnO_2 NRs agrees well with the atomic model. The exposed {110} facets is calculated to be $\sim 96\%$ by using {110}/[{001} + {110}]. Thus, we conclude that SnO_2 NRs are mainly exposed with {110} facets.

Fig. 5(a) presents a typical BF TEM image of SnO_2 NPs. It clearly shows that the size of the NPs is 5–10 nm, which is consistent with the XRD and SEM results. Moreover, the congregation phenomenon of NPs is also found. The SAED pattern (inset in **Fig. 5(a)**) exhibits homocentric rings, which can be unambiguously attributed to the fact that the NPs are polycrystalline. **Fig. 5(b)** shows a typical HRTEM image of single nanoparticle (NP), from which the (110) lattice spacing is measured to be 3.35 Å, consistent with that of bulk SnO_2 .

Fig. 6(a) shows a typical BF TEM image, illustrating that 3D SnO_2 nanostructures are composed of DNCs. The inset in **Fig. 6(a)** is the corresponding SAED pattern, which can be indexed to tetragonal SnO_2 . According to the above SEM and TEM observations, we propose a model of an ideal dodecahedral SnO_2 enclosed by four side facets and eight parallelogram facets, as shown in **Fig. 6(b)**. **Fig. 6(c)** shows a typical [010] zone-axis HRTEM image of an individual SnO_2 dodecahedral nanocrystal (DNC). This HRTEM image clearly shows that the eight parallelogram facets are identified as {101} facets. It can be seen the outline and angle marked in **Fig. 6(c)** of SnO_2 DNC agree with the model of an ideal dodecahedral SnO_2 enclosed by {110} and {101} facets projected along [010] direction (**Fig. 6(d)**). HRTEM image of SnO_2 DNC was taken along [110] direction to further confirm the exposed facets of the SnO_2 DNC. As shown in **Fig. 6(e)**, the outline of the SnO_2 DNC viewed along [110] direction is consistent with the dodecahedral SnO_2 model projected along the same direction (**Fig. 6(f)**). Based on the above TEM observations and structural analyses, we can deduce that the SnO_2 DNCs possess exposed facets of {110} and {101}.

3.2. Humidity sensing properties

The humidity-sensing properties were carried out on the sensor devices obtained from the as-synthesized SnO_2 nanostructures at a frequency of 100 Hz. The response and recovery times are two key factors to evaluate the performance of a humidity sensor [27,28], in which a sensor achieves 90% of the total impedance change in the case of adsorption and desorption, respectively. **Fig. 7** shows the response and recovery curves of the sensors based on various SnO_2 nanostructures as the RH switches between 11% and 95% at 25 °C. For the nanosensor based on SnO_2 NPs, it has long response and recovery times ($t > 30$ s), indicating that it will take a long time to reach a stable state. However, the nanosensors based on 3D hierarchical SnO_2 NRs and DNCs possess a response time of less than 4 s and a recovery time of less than 13 s. This reveals that the 3D SnO_2 nanostructures (NRs and DNCs) have faster response and recovery times compared with SnO_2 NPs, which are attributed to the peculiar 3D open nanostructures with more pore channels. That is to say, when the nanosensors based on 3D hierarchical SnO_2 NRs and DNCs are placed in a high RH environment, the 3D open nanostructures can facilitate the diffusion of water molecules through the numerous channels formed by voids and interspaces, and accelerate the formation of steady state of nanosensors [29]. Thus, the 3D hierarchical SnO_2 NRs and DNCs-based nanosensors display fast response

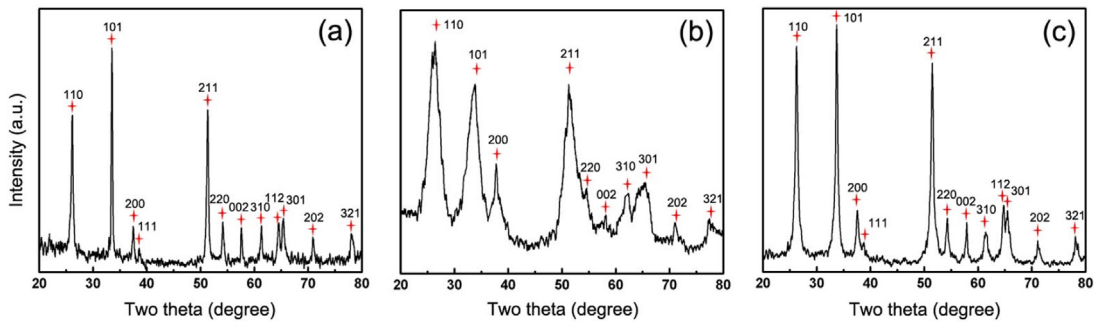


Fig. 1. XRD patterns of as-synthesized 3D hierarchical SnO₂ NRs (a), SnO₂ NPs (b) and 3D hierarchical SnO₂ DNCs (c).

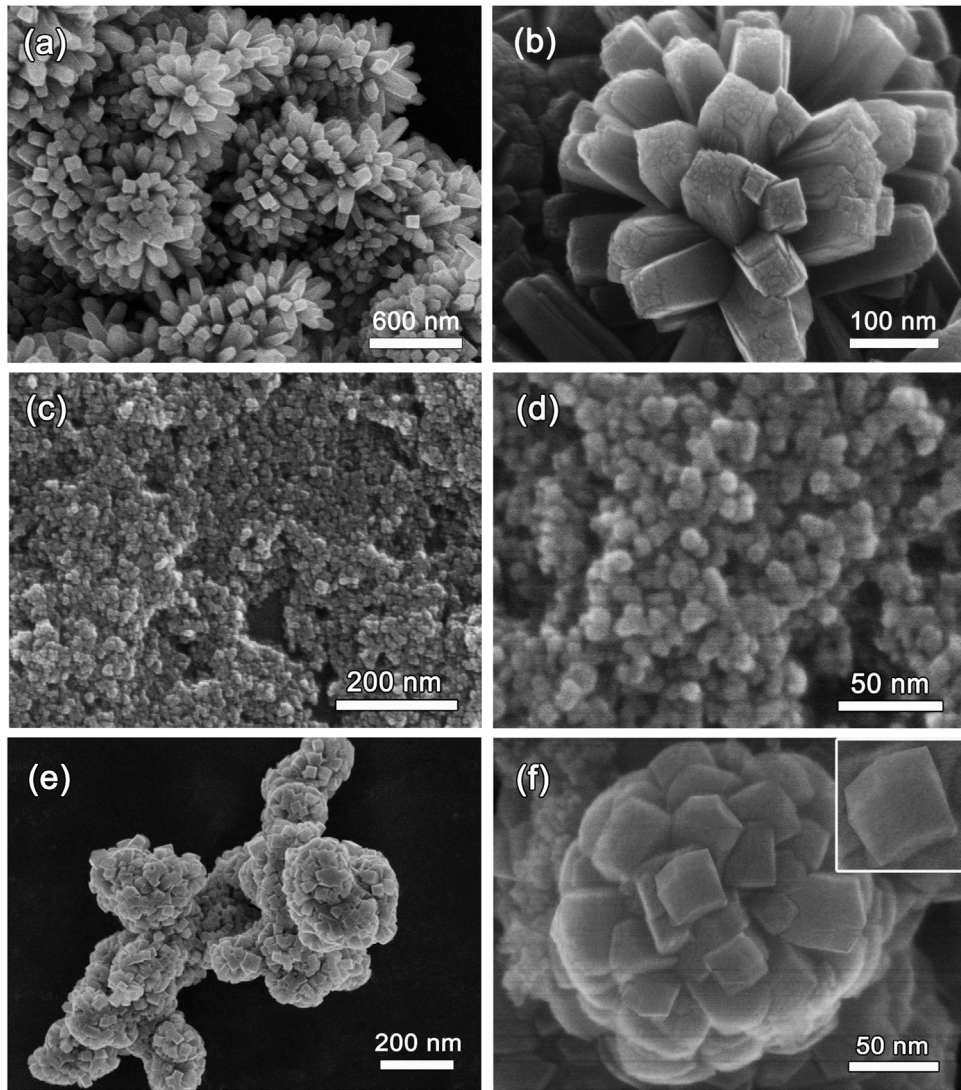


Fig. 2. SEM images of as-synthesized 3D hierarchical SnO₂ NRs (a), SnO₂ NPs (c), and 3D hierarchical SnO₂ DNCs (e); (b), (d) and (f) the corresponding SEM images at high magnification.

times when the RH changes from 11% to 95%. In contrast, when putting those nanosensors in a low RH environment immediately, the adsorbed water molecules on the SnO₂ surface can be desorbed rapidly to cut off the water channels for proton transfers. Therefore, fast recovery times are observed on the nanosensors based on 3D hierarchical SnO₂ NRs and DNCs. However, for the nanosensor based on SnO₂ NPs, the congregation phenomena of the NPs hinders the movement and diffusion of water molecules [29], thus prolong-

ing the response and recovery times. Based on the above analyses, we conclude that the humidity sensors realized with 3D hierarchical SnO₂ NRs and DNCs exhibit faster response and recovery times than that based on SnO₂ NPs.

Fig. 8(a) shows the dependence of impedance on different RHs for the nanosensors based on different SnO₂ nanostructures. When the RH is changed from 11% to 95%, the 3D hierarchical SnO₂ NRs and NPs exhibit poor responses on impedance changes, dropping

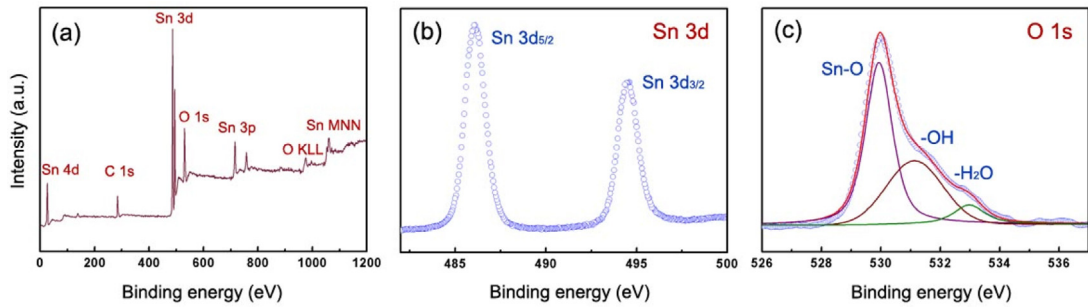


Fig. 3. (a) XPS spectra of 3D hierarchical SnO_2 DNCs scanned from 0 to 1200 eV; Binding energies of Sn 3d (b) and O 1s (c).

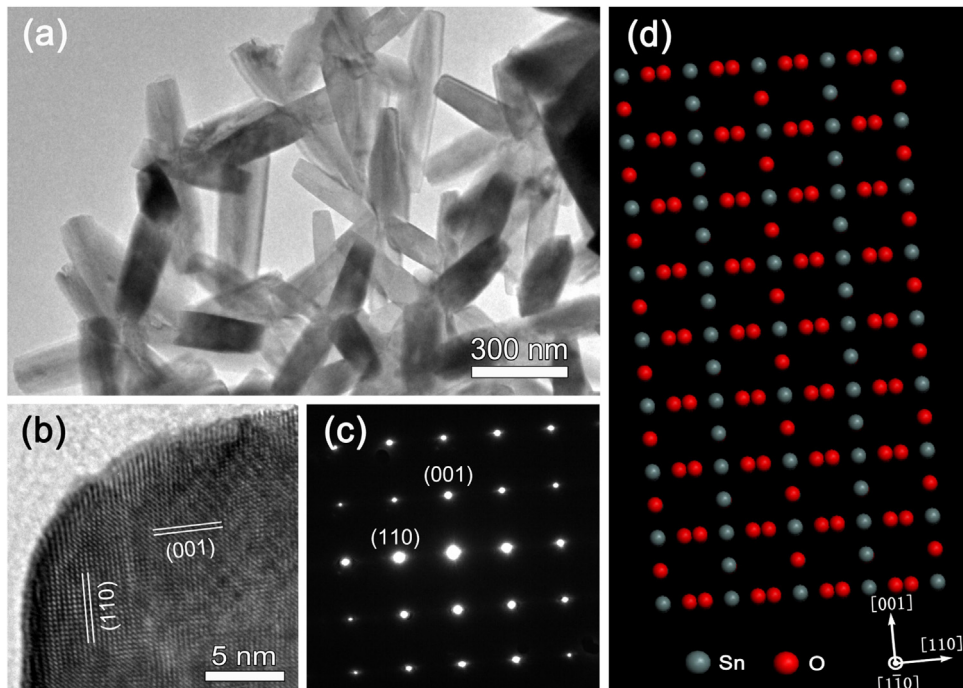


Fig. 4. (a) Typical BF TEM image of 3D hierarchical SnO_2 NRs; (b) HRTEM image of an individual NR viewed along $[1\bar{1}0]$ direction; (c) SAED pattern taken from the NR in (b); (d) Schematic model of an ideal SnO_2 cuboid projected along $[1\bar{1}0]$ direction.

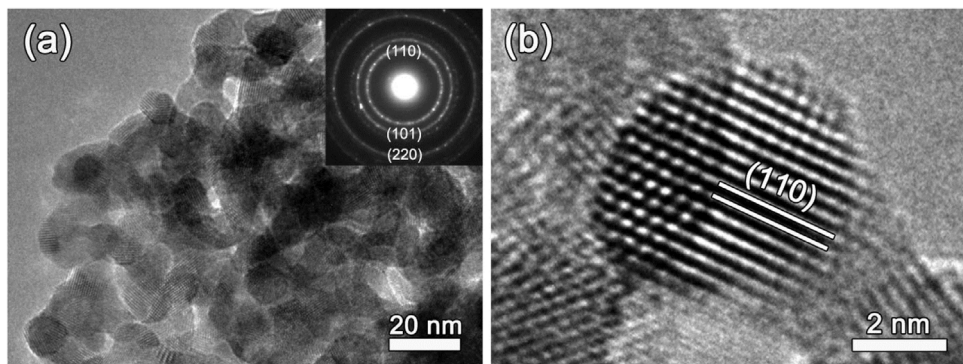


Fig. 5. (a) Typical BF TEM image of SnO_2 NPs, and inset is corresponding SAED pattern; (b) Typical HRTEM image of single SnO_2 NP.

by only one and two orders, respectively. However, the nanosensor based on 3D hierarchical DNCs displays an excellent linearity with the log(impedance) spanning nearly 4.2 orders of magnitude,

indicating that its humidity sensitivity is much higher than those based on SnO_2 NRs and NPs.

To see the humidity sensing performance of the nanosensors based on SnO_2 DNCs more clearly, we made a comparison of the

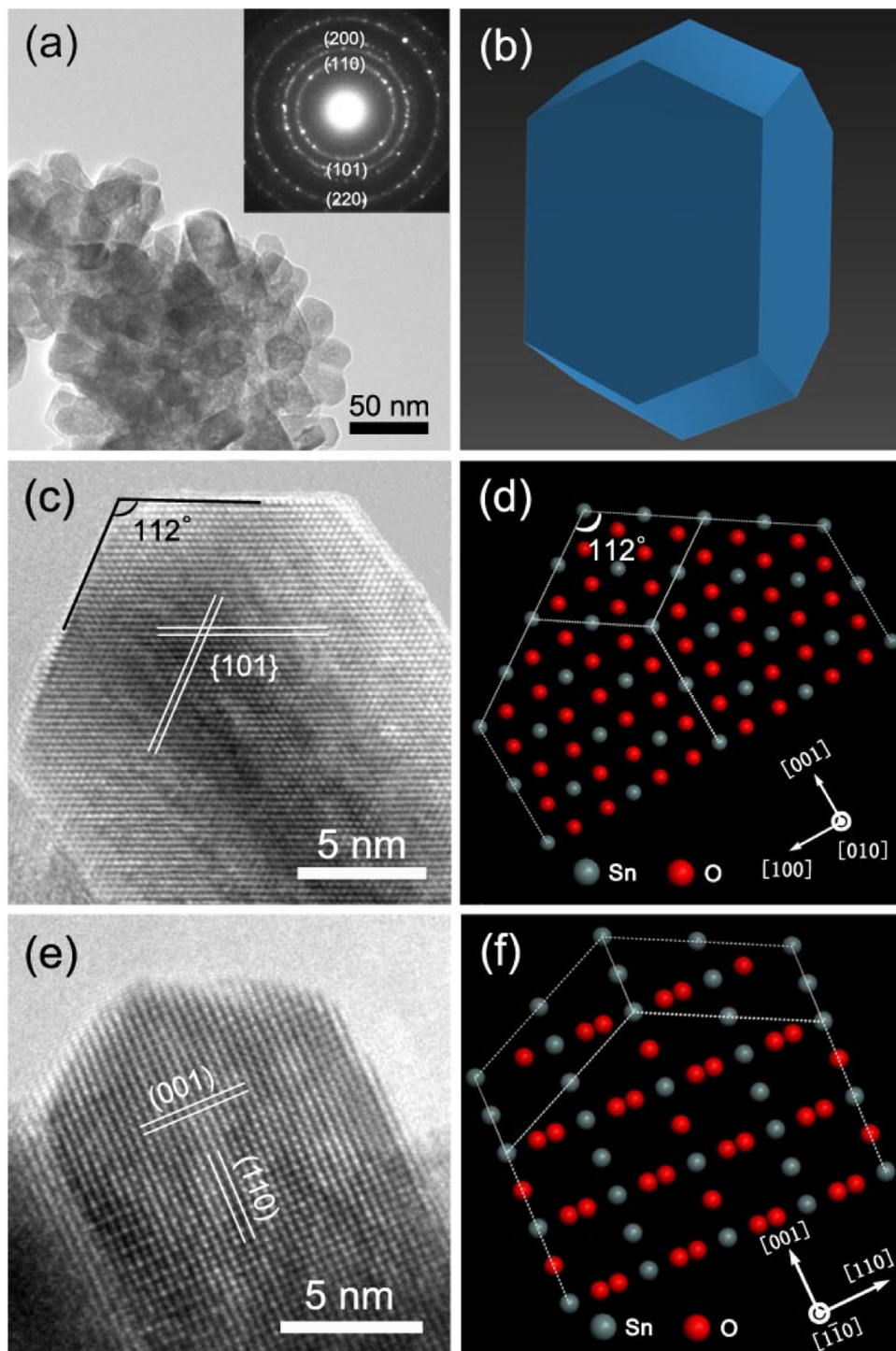


Fig. 6. (a) Typical BF TEM image of SnO₂ DNCs. Inset is SAED pattern; (b) Schematic model of an ideal SnO₂ dodecahedron; (c) Typical HRTEM image for the SnO₂ dodecahedron viewed along the [010] direction; (d) Schematic model of an ideal SnO₂ dodecahedron projected along [010] direction; (e) Typical HRTEM image viewed along the [1-10] direction; (f) Schematic model of an ideal SnO₂ dodecahedron projected along [1-10] direction.

nanosensors reported in the literature and in the present study, as summarized in Table 1. It is clearly shown that humidity nanosensor based on SnO₂ DNCs exhibits fast response/recovery times and high sensitivity, which are superior to those based on metal oxides reported in the previous literature.

Hysteresis is another important characteristic of a humidity sensor, which is defined as the maximum difference between the adsorption and desorption processes [13]. Generally speaking, a sensing material experiences a hysteresis effect at increasing and

decreasing RH. The hysteresis was measured by switching the sensor between the closed chambers with RHs of 11%, 33%, 43%, 54%, 69%, 75%, 84% and 95% and then transferred back. The humidity hysteresis deviation (γ_H) was calculated using the equation as follows,

$$\gamma_H = \pm \frac{\Delta R_{\max}}{2F_{Fs}} \quad (1)$$

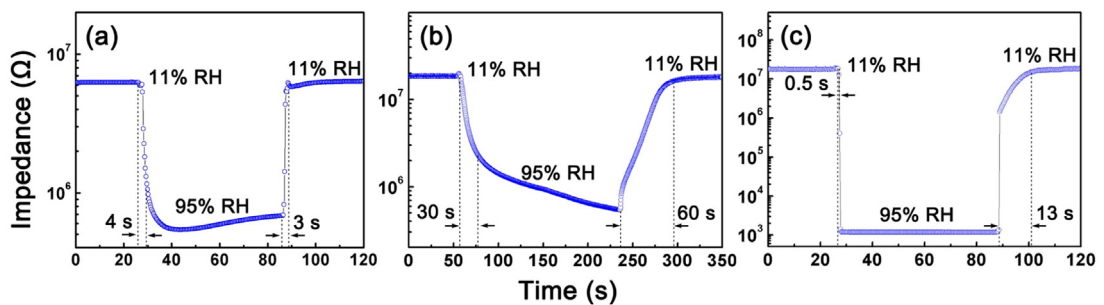


Fig. 7. Humidity response and recovery curves for 3D hierarchical SnO₂ NRs (a), SnO₂ NPs (b) and 3D hierarchical SnO₂ DNCs (c).

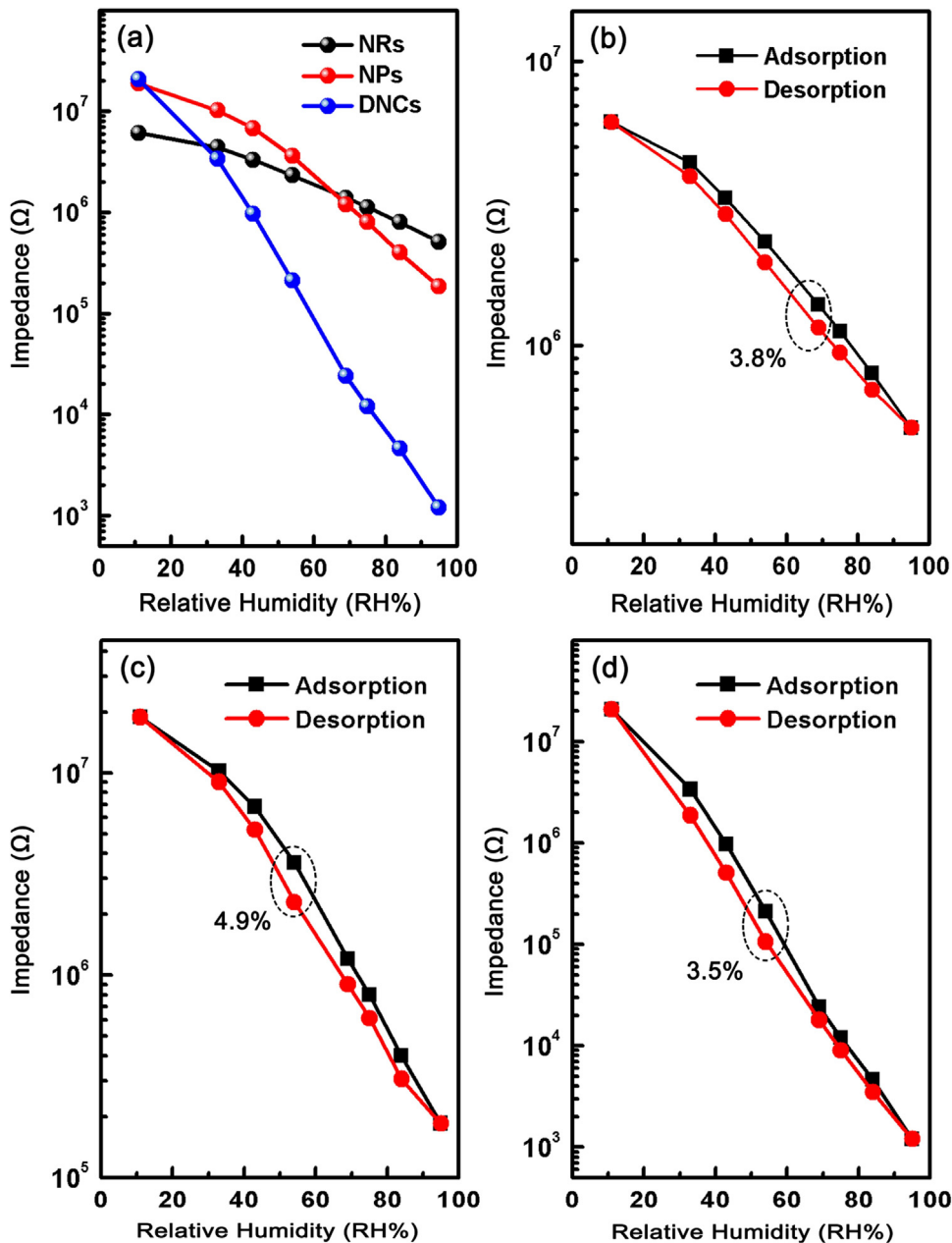


Fig. 8. Impedance measurement of nanosensors fabricated from different SnO₂ nanostructures (a). The humidity hysteresis characteristics of the nanosensors based on 3D hierarchical SnO₂ NRs (b), SnO₂ NPs (c) and 3D hierarchical SnO₂ DNCs (d).

Table 1

Comparison of the sensing properties for various humidity sensors.

Materials	Impedance variation (Ω)	Response time (s)	Recovery time (s)	Reference
Single SnO ₂ nanowires	10^5 – 10^7	120–170	20–60	[12]
SnO ₂ NPs	10^2 – 10^4	32	25	[14]
TiO ₂ –SnO ₂ nanowires	10^4 – 10^7	2.4	30	[15]
WO ₃ –SnO ₂ nanospheres	–	8	29	[16]
RGO–SnO ₂ nanocomposite	–	6	102	[17]
ZrO ₂ –TiO ₂ nanofibers	10^4 – 10^8	5	20	[29]
MoS ₂ –SnO ₂ nanocomposite	–	5	13	[30]
3D hierarchical SnO ₂ DNCs	10^3 – 10^7	0.5	13	this work

where ΔR_{\max} is the output difference between forward and backward operations and F_F is the full scale output. Fig. 8 shows the impedance measurements of humidity nanosensors realized with different SnO₂ nanostructures. Among the as-fabricated nanosensors, the 3D hierarchical DNCs nanosensor exhibits a narrowest hysteresis loop with a calculated maximum deviation of 3.5% (Fig. 8(d)), indicating that the adsorption and desorption processes are highly reversible.

3.3. Humidity-sensing mechanism

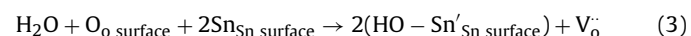
To further understand the sensing mechanism, the complex impedance measurements of the nanosensors based on SnO₂ nanostructures were carried out through shifting the operational frequency from 50 Hz to 100 kHz under different RHs. As shown in Fig. 9(a), the complex impedance curves of 3D hierarchical SnO₂ NRs present one type of shape, in which semicircular curves appear for the RHs from 11% to 95%. The semicircle represents the “non-debye” relation [30], which can be modeled by an equivalent circuit of a resistor (R) and a constant phase element (CPE, Z_{CPE}) in parallel, as shown in Fig. 9(d). These observed semicircles are attributed to the intrinsic impedance [31], indicating only a few water molecules are chemisorbed and a few channels form on the surfaces of SnO₂ nanostructures for the proton transport. However, two types of signals are shown in the complex impedance spectra of the nanosensors based on 3D hierarchical SnO₂ DNCs and SnO₂ NPs. As can be seen from Fig. 9(b) and (c) the complex impedance curves exhibit a semicircle at low RH, and a semicircle together with a straight line at high RH, respectively. The straight line represents Warburg impedance due to the diffusion and transport of protons in the adsorbed water [13]. To model the complex impedance plots of the nanosensors based on NPs and 3D hierarchical SnO₂ DNCs, the equivalent circuits of are depicted in Fig. 9(e) and (f), respectively. Herein, Z_w is introduced to represent the Warburg impedance [31], which implies that many water molecules are adsorbed on the surfaces of SnO₂ DNCs and NPs, leading to formation of several water layers and thus producing numerous water channels distributed in 3D hierarchical SnO₂ DNCs and SnO₂ NPs. The adsorbed water layers exhibit a liquid-like behavior, in which proton hopping occurs in the charge transport by a chain reaction [31] between adjacent water molecules as follows,



The free transfer of proton in the water layer results in an impedance decrease for the nanosensors based on 3D hierarchical SnO₂ DNCs and SnO₂ NPs. From the above complex impedance results, it is concluded that the 3D hierarchical SnO₂ DNCs and SnO₂ NPs can adsorb more water molecules than the 3D hierarchical SnO₂ NRs, which leads to higher sensitivity of nanosensors based on the 3D hierarchical SnO₂ DNCs and SnO₂ NPs. The analyses of XPS spectra obtained from different SnO₂ nanostructures confirm that only a few OH groups and water molecules are adsorbed to form water layers on the surfaces of SnO₂ NRs, in contrary to DNCs and

NPs. That is why NR sensor is characterized with lack of Warburg impedance, as shown in Fig. 9.

It is well known that the surface structure strongly affects the adsorption behavior of materials [8]. According to our TEM results, the 3D hierarchical SnO₂ NRs are mainly exposed with {110} facets, while for the 3D hierarchical SnO₂ DNCs, apart from {110} facets, {101} facets are also exposed. To understand the adsorption mechanism of different surfaces, DFT calculations were performed to investigate adsorption behaviors of OH groups on SnO₂ {110} and {101} surfaces. When SnO₂ nanostructures are exposed to a high amount of moisture, water molecules adsorbed on the SnO₂ surface will react with the lattice oxygen (O_{Osurface}) and the surface tin atoms (Sn_{Snsurface}) according to the following reaction,



HO-Sn'_{Snsurface} forms on the surface of SnO₂ and V_o (oxygen vacancy) is generated at the same time [27]. Here Sn'_{Snsurface} is the surface tin atom after the reaction, which is coordinatively unsaturated with one dangling bond.

Fig 10(a) and (b) shows the optimized adsorption configurations of OH groups on SnO₂ {110} and {101} surfaces, respectively. It can be seen that, the number of OH groups adsorbed on Sn atom of the SnO₂ {101} surface are two times that on {110} surface. For the {110} surface, the OH group is only adsorbed on the bridge site in the middle of two surface Sn atoms. While for {101} surface, besides the bridge sites, OH groups are also adsorbed on Sn atoms owing to the high density of atomic steps on the {101} surface, which is consistent with the XPS results. The OH groups are considered as active sites for the adsorption of water molecules [15], which will greatly improve the humidity sensitivity of nanosensors. Thus, 3D hierarchical SnO₂ DNCs enclosed with {101} facets and {110} facets exhibit higher sensitivity in comparison with 3D hierarchical SnO₂ NRs with exposed {110} facets.

Fig. S4 shows the N₂ adsorption-desorption isotherms of different SnO₂ nanostructures. From the BET measurements in Figs. S4(a)–(c), the specific surface area for the NPs (173.6 m²/g) is more than that for DNCs (23.9 m²/g) and NRs (7.9 m²/g). Figs. S4(d)–(f) present the pore size distribution curves of SnO₂ nanostructures. The pore diameters are calculated to be 34.5 nm, 5.0 nm and 15.8 nm for SnO₂ NRs, NPs and DNCs, respectively. Although the BET specific surface area of SnO₂ NPs is 7 and 22 times that of 3D hierarchical SnO₂ DNCs and NRs, the pore size of NPs is smallest among three different SnO₂ nanostructures. This can be attributed to the pore blockage due to the congregation of NPs which is believed to obstruct the reaction of water molecules with the inner sensing material [32], thus hindering the formation of OH groups and adsorption of water molecules. That is why nanosensor based on 3D hierarchical SnO₂ DNCs is more sensitive than that based on NPs.

Fig. 11 shows the dynamic response of SnO₂ DNCs sensor towards rapid variations in the 11–95% RH range. It is observed from Fig. 11(a) that the impedance of the sensor always reverts to the original value when RH is changed to the former state, indicating that the humidity-sensing process is extremely reversible.

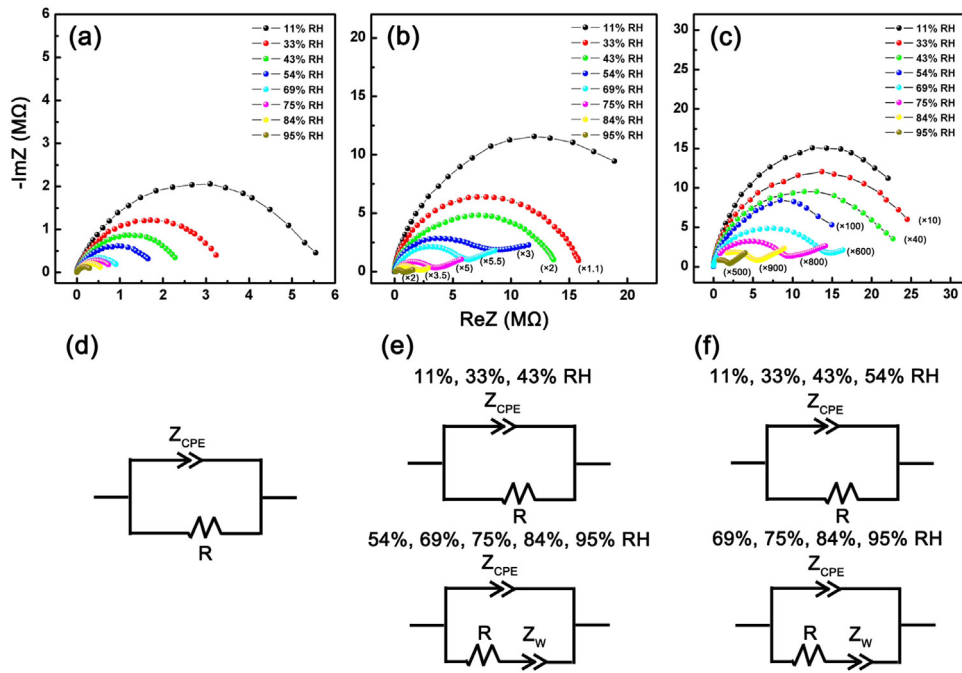


Fig. 9. Complex impedance plots of the as-fabricated nanosensors based on 3D hierarchical SnO_2 NRs (a), SnO_2 NPs (b) and 3D hierarchical SnO_2 DNCs (c). Equivalent circuits of the nanosensors based on 3D hierarchical SnO_2 NRs (d), SnO_2 NPs (e) and 3D hierarchical SnO_2 DNCs (f).

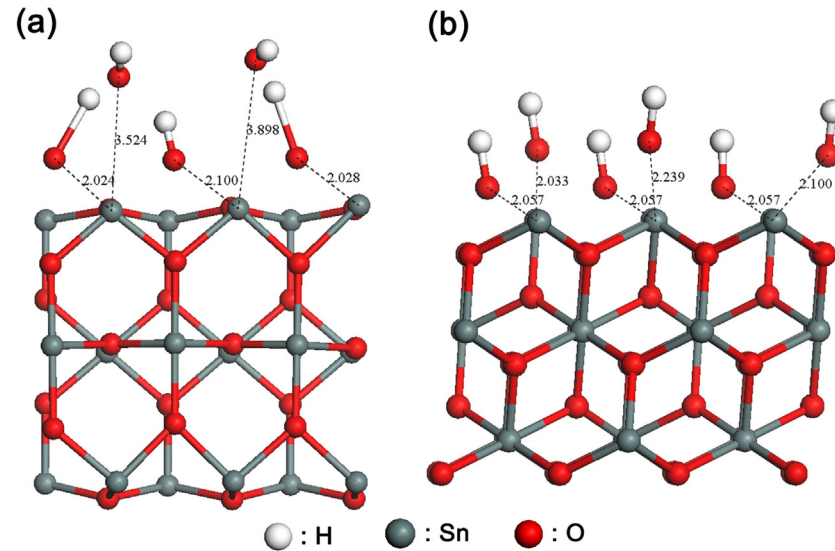


Fig. 10. Adsorption behaviors of OH groups on {110} surface (a) and {101} surface (b).

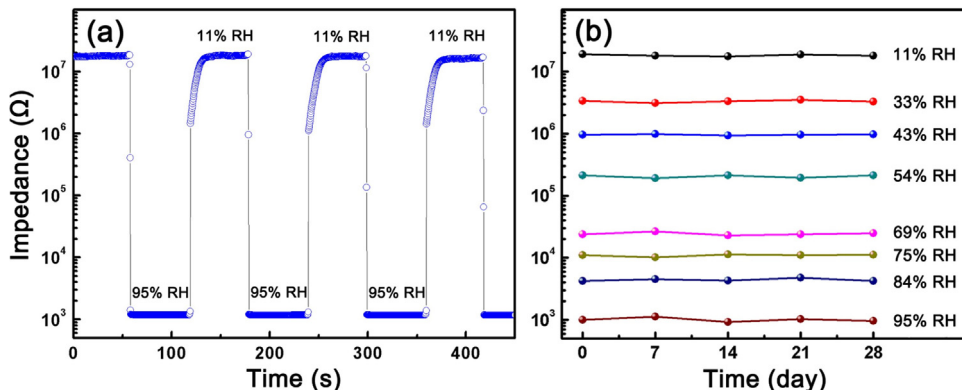


Fig. 11. (a) Repeated response and recovery characteristics of 3D hierarchical SnO_2 DNCs. (b) The responses of 3D hierarchical SnO_2 DNCs monitored at different humidity conditions for 28 days.

Moreover, the response and recovery times do not change during the four repeated loops of measurements, implying a good reproducibility of the humidity response. The sensors were exposed in air for 28 days, and the impedance measurement was performed once a week at different RHs. As can be seen in Fig. 11(b), the impedance of the sensor fluctuates slightly with time. The sensor shows excellent consistency and a minor variation (~2.1%) in impedance is observed at each humidity level.

4. Conclusions

In summary, 3D hierarchical SnO₂ DNCs with exposed {110} and {101} facets were synthesized by a simple hydrothermal route with assistance of sodium alginate. The 3D hierarchical SnO₂ DNCs show excellent humidity-sensing performance including fast response and recovery times, narrow hysteresis loop, high sensitivity, great linearity response and good stability due to the unique 3D open structure and high chemical activity of the exposed {101} facets. Our results demonstrate that it is feasible to improve humidity-sensing properties of SnO₂ sensors by tuning morphology and surface architecture. In addition, the present study motivates us to further explore new synthetic method for the preparation of other metallic oxides with special morphology and high active facets, which could demonstrate promising application prospects in gas sensing, photocatalysis, lithium-ion batteries and optoelectronic devices.

Acknowledgements

The authors would like to thank the financial support from the National Key Basic Research Development Program of China (Grant no.: 2012CB722705), the Natural Science Foundation for Outstanding Young Scientists in Shandong Province (Grant no.: JQ201002) and High-end Foreign Experts Recruitment Program (Grant nos.: GDW20163500110, GDW20143500163). Y. Q. Wang would also like to thank the financial support from the Top-notch Innovative Talent Program of Qingdao City (Grant no.: 13-CX-8), and the Taishan Scholar Program of Shandong Province, China.

Appendix A. Supplementary data

Supplementary data associated with this article can be found, in the online version, at <http://dx.doi.org/10.1016/j.snb.2016.12.043>.

References

- [1] C. Sun, K.R.G. Karthik, S.S. Pramana, L.H. Wong, J. Zhang, Y. Huang, C.H. Sow, N. Mathews, S.G. Mhaisalkar, The role of tin oxide surface defects in determining nanonet FET response to humidity and photoexcitation, *J. Mater. Chem. C* 2 (2014) 940–945.
- [2] D.Z. Zhang, J. Tong, B.K. Xia, Humidity-sensing properties of chemically reduced graphene oxide/polymer nanocomposite film sensor based on layer-by-layer nano self-assembly, *Sens. Actuators B* 197 (2014) 66–72.
- [3] D.Z. Zhang, J. Tong, B.K. Xia, Q.Z. Xue, Ultrahigh performance humidity sensor based on layer-by-layer self-assembly of graphene oxide/polyelectrolyte nanocomposite film, *Sens. Actuators B* 203 (2014) 263–270.
- [4] X.L. He, D.J. Li, J. Zhou, W.B. Wang, W.P. Xuan, S.R. Dong, H. Jin, J.K. Luo, High sensitivity humidity sensors using flexible surface acoustic wave devices made on nanocrystalline ZnO/polyimide substrates, *J. Mater. Chem. C* 1 (2013) 6210–6215.
- [5] X.Q. Fu, C. Wang, H.C. Yu, Y.G. Wang, T.H. Wang, Fast humidity sensors based on CeO₂ nanowires, *Nanotechnology* 18 (2007) 145503.
- [6] A. Zainelabdin, G. Amin, S. Zaman, O. Nur, J. Lu, L. Hultman, M. Willander, CuO/ZnO nanocorals synthesis via hydrothermal technique: growth mechanism and their application as humidity sensor, *J. Mater. Chem.* 22 (2012) 11583–11590.
- [7] Z.Y. Li, H.N. Zhang, W. Zheng, W. Wang, H.M. Huang, C. Wang, A.G. MacDiarmid, Y. Wei, Highly sensitive and stable humidity nanosensors based on LiCl doped TiO₂ electrospun nanofibers, *J. Am. Chem. Soc.* 130 (2008) 5036–5037.
- [8] X.G. Han, M.S. Jin, S.F. Xie, Q. Kuang, Z.Y. Jiang, Y.Q. Jiang, Z.X. Xie, L.S. Zheng, Synthesis of tin dioxide octahedral nanoparticles with exposed high-energy {221} facets and enhanced gas-sensing properties, *Angew. Chem. Int. Ed.* 48 (2009) 9180–9183.
- [9] D.Z. Zhang, A.M. Liu, H.Y. Chang, B.K. Xia, Room-temperature high-performance acetone gas sensor based on hydrothermal synthesized SnO₂-reduced graphene oxide hybrid composite, *RSC Adv.* 225 (2015) 3016–3022.
- [10] X.S. Zhou, L.J. Wan, Y.G. Guo, Binding SnO₂ nanocrystals in nitrogen-doped graphene sheets as anode materials for lithium-ion batteries, *Adv. Mater.* 25 (2013) 2152–2157.
- [11] A. Kar, A. Patra, Recent development of core-shell SnO₂ nanostructures and their potential applications, *J. Mater. Chem. C* 2 (2014) 6706–6722.
- [12] Q. Kuang, C.S. Lao, Z.L. Wang, Z.X. Xie, L.S. Zheng, High-sensitivity humidity sensor based on a single SnO₂ nanowire, *J. Am. Chem. Soc.* 129 (2007) 6070–6071.
- [13] V.K. Tomer, S. Duhan, In-situ synthesis of SnO₂/SBA-15 hybrid nanocomposite as highly efficient humidity sensor, *Sens. Actuators B* 212 (2015) 517–525.
- [14] M. Parthibavarman, V. Hariharan, C. Sekar, High-sensitivity humidity sensor based on SnO₂ nanoparticles synthesized by microwave irradiation method, *Mater. Sci. Eng. C* 31 (2011) 840–844.
- [15] Z.L. Yang, Z.Y. Zhang, K.C. Liu, Q. Yuan, B. Dong, Controllable assembly of SnO₂ nanocubes onto TiO₂ electrospun nanofibers toward humidity sensing applications, *J. Mater. Chem. C* 3 (2015) 6701–6708.
- [16] H. Li, B. Liu, D.P. Cai, Y.R. Wang, Y. Liu, L. Mei, L.L. Wang, D.D. Wang, Q.H. Li, T.H. Wang, High-temperature humidity sensors based on WO₃-SnO₂ composite hollow nanospheres, *J. Mater. Chem. A* 2 (2014) 6854–6862.
- [17] D.Z. Zhang, H.Y. Chang, P. Li, R.H. Liu, Q.Z. Xue, Fabrication and characterization of an ultrasensitive humidity sensor based on metal oxide/graphene hybrid nanocomposite, *Sens. Actuators B* 225 (2016) 233–240.
- [18] H. Wang, Q.Q. Liang, W.J. Wang, Y.R. An, J.H. Li, L. Guo, Preparation of flower-like SnO₂ nanostructures and their applications in gas-sensing and lithium storage, *Cryst. Growth Des.* 11 (2011) 2942–2947.
- [19] Q.Q. Zhao, D.X. Ju, X.L. Deng, J.Z. Huang, B.Q. Cao, X.J. Xu, Morphology-modulation of SnO₂ hierarchical architectures by Zn doping for glycol gas sensing and photocatalytic applications, *Sci. Rep.* 5 (2015) 7874.
- [20] B. Delley, Fast calculation of electrostatics in crystals and large molecules, *J. Phys. Chem.* 100 (1996) 6107–6110.
- [21] B. Delley, From molecules to solids with the DMol³ approach, *J. Chem. Phys.* 113 (2000) 7756–7764.
- [22] J.P. Perdew, K. Burke, M. Ernzerhof, Generalized gradient approximation made simple, *Phys. Rev. Lett.* 77 (1996) 3865–3868.
- [23] Y. Inada, H. Orita, Efficiency of numerical basis sets for predicting the binding energies of hydrogen bonded complexes: evidence of small basis set superposition error compared to Gaussian basis sets, *J. Comput. Chem.* 29 (2008) 223–232.
- [24] B. Delley, Hardness conserving semilocal pseudopotentials, *Phys. Rev. B* 66 (2002) 155125.
- [25] S.S. Wu, H.Q. Cao, S.F. Yin, X.W. Liu, X.R. Zhang, Amino acid-assisted hydrothermal synthesis and photocatalysis of SnO₂ nanocrystals, *J. Phys. Chem. C* 113 (2009) 17893–17898.
- [26] K.W. Liu, M. Sakurai, M. Aono, One-step fabrication of β-Ga₂O₃-amorphous-SnO₂ core-shell microribbons and their thermally switchable humidity sensing properties, *J. Mater. Chem.* 22 (2012) 12882–12887.
- [27] T. Fu, J. Zhu, M. Zhuo, B.K. Guan, J.D. Li, Z. Xu, Q.H. Li, Humidity sensors based on graphene/SnO₂/CF nanocomposites, *J. Mater. Chem. C* 2 (2014) 4861–4866.
- [28] F. Ménil, M. Susbielles, H. Débédé, C. Lucat, P. Tardy, Evidence of a correlation between the non-linearity of chemical sensors and the asymmetry of their response and recovery curves, *Sens. Actuators B* 106 (2005) 407–423.
- [29] M.Y. Su, J. Wang, H.Y. Du, P.J. Yao, Y.G. Zheng, X.G. Li, Characterization and humidity sensitivity of electrospun ZrO₂:TiO₂ hetero-nanofibers with double jets, *Sens. Actuators B* 161 (2012) 1038–1045.
- [30] D.Z. Zhang, Y. Sun, P. Li, Y. Zhang, Facile fabrication of MoS₂-modified SnO₂ hybrid nanocomposite for ultrasensitive humidity sensing, *ACS Appl. Mater. Interfaces* 8 (2016) 14142–14149.
- [31] V.K. Tomer, S. Devi, R. Malik, S.P. Nehra, S. Duhan, Fast response with high performance humidity sensing of Ag-SnO₂/SBA-15 nanohybrid sensors, *Microporous Mesoporous Mater.* 219 (2016) 240–248.
- [32] Z.Y. Zhang, J.D. Huang, Q. Yuan, B. Dong, Intercalated graphitic carbon nitride: a fascinating two-dimensional nanomaterial for an ultrasensitive humidity nanosensors, *Nanoscale* 6 (2014) 9250–9256.

Biographies

Honglei Feng received his B.S. degree from Qingdao University in 2014. Currently, he is graduate student at Qingdao University, Qingdao, China. His fields of interests include functional materials and humidity sensors.

Chen Li received B.S. degree from Qingdao University in 2015. Currently, he is graduate student at Qingdao University, Qingdao, China. His fields of interests are sensing materials and functional nanomaterials.

Tao Li is a doctoral student in the College of Physics, Qingdao University, China. His current scientific interests are functional nanomaterials.

Feiyu Diao is a doctoral student in the College of Physics, Qingdao University, China. Her current scientific interests are nano photoelectric materials.

Tuo Xin received his B.S. degree from China University of Petroleum (East China) in 2015. Currently, he is graduate student at Qingdao University. His fields of interests include functional nanomaterials-based sensors and lithium ion anode materials.

Bin Liu received his B.S. degree from Qingdao University in 2014. Currently, he is a graduate student of Qingdao University, Qingdao, China. His fields of interests include the microstructure and physical properties of functional perovskite thin films.

Yiqian Wang received his Ph.D. degree in condensed matter physics from Institute of Physics, Chinese Academy of Sciences, in 2001, and performed research fellow at Imperial College London, UK and INRS-EMT, Canada. He is currently a professor at Qingdao University. His research interest includes the fabrication and characterization of perovskite film materials, nano optoelectronic materials, and sensing materials, as well as to exploit their potential applications.